

Simultaneous non-contact identification of the elastic modulus, damping and coefficient of thermal expansion in 3D-printed structures

Gašper Krivic, Janko Slavič*

University of Ljubljana, Faculty of Mechanical Engineering, Aškerčeva 6, Ljubljana, 1000, Slovenia

ARTICLE INFO

Keywords:

Elastic modulus
Coefficient of thermal expansion
Damping ratio
Glass-transition temperature
3D printing
Electrothermal actuators

ABSTRACT

Thermoplastic-extrusion 3D printing has gained popularity for the fabrication of electrothermal soft actuators that can control shape in response to temperature changes generated by embedded 3D-printed heaters. However, the material properties, such as the coefficient of thermal expansion, elastic modulus, and damping, significantly impact the performance of these 3D-printed electrothermal actuators. The material properties can be temperature-dependent, and vary based on the print and fill orientation. Current experimental methods cannot simultaneously research these properties, resulting in partial research of the influencing parameters.

This research introduces a simultaneous and non-contact identification method for the elastic modulus, damping, and coefficient of thermal expansion, utilizing optical and thermal cameras, a scanning laser vibrometer, IR heating, and electrodynamic shaker excitation. The method was applied to several materials, including composites. The introduced method can fully characterize the 3D prints and the materials used for 3D printing, leading to the faster and more predictable development of future 3D-printed electrothermal actuators.

1. Introduction

Smart structures sense changes in the environment and react accordingly in real time [1]. Multimaterial 3D printing has enabled the fabrication of smart structures [2,3], sensors [4,5] and actuators [6,7]. Fully 3D-printed soft actuators can be manufactured in a single process [8] and therefore custom designs are much more viable, when compared to semi-3D-printed counterparts that require skilled operators and post-processing assembly [9]. Unlike conventional actuators, soft actuators produce flexible motion due to the integration of microscopic changes at the molecular level into a macroscopic deformation of the actuator material [10]. Soft actuators can be classified into several subgroups based on their actuation mechanisms, such as piezoelectric [11], dielectric [6], magnetic [12], electrostatic [13], pneumatic [14], thermal [15], electrothermal [16], and shape memory [17].

The bimorph electrothermal actuator is probably the oldest and best electrothermal actuator design [18]. It consists of two or more layers of different materials and a resistive heater between them. Electricity generates Joule heat and the difference in the coefficient of thermal expansion (CTE) of the layers causes deflection. Joule heating uses comparatively low drive voltages, but can produce large forces and displacements [19]. For this reason, bimorph electrothermal actuators have attracted much attention in the field of soft robotics for

joints [20], grippers [21,22], small crawling soft robots [23,24] and robot fingers [25], and in electronics for switches [26].

Chu et al. [27] developed an analytical model for the electromechanical performance of a bimetallic cantilever beam. They showed that the tip deflection and force of a bimorph electrothermal actuator depend on the elastic modulus and the CTE of the materials used. In addition, damping properties are also important, because soft actuators are mainly made of soft elastic materials, resulting in large oscillations in the actuation and de-actuation, or in rapid motion [28,29]. In 3D-printed bimorph actuators the elastic modulus, damping, and CTE are influenced by a number of parameters, including print orientation and fill angle, see Popescu et al. [30]. The elastic modulus, damping and CTE also differ with the material used for 3D printing.

Some of the most commonly used commercially available materials for thermoplastics-extrusion 3D printing are polylactic acid (PLA), polyethylene terephthalate glycol (PETG), thermoplastic polyurethane (TPU) and nylon/polyamide (PA) [31]. Recent advances in materials science have made it possible to use thermoplastic composite materials for 3D printing [32]. In composite materials, reinforcements are added to the matrix in the form of particles [33–35], short fibers [36,37], continuous fibers [38], and nanoparticles [39,40] to enhance mechanical properties such as elastic modulus, damping and CTE. Therefore, to fully understand the behavior and potential applications for bimorph

* Corresponding author.

E-mail addresses: gasper.krivic@fs.uni-lj.si (G. Krivic), janko.slavic@fs.uni-lj.si (J. Slavič).

actuators, it is essential to accurately characterize the elastic modulus, damping, and CTE of the materials for 3D printing.

The most common method for testing the elastic modulus of 3D-printed structures is the tensile test. For example, Zhao et al. [41] and Yao et al. [42] used tensile tests to evaluate the elastic modulus of PLA for different print orientations and layer heights. In addition, Liu et al. [43] tested PLA composite materials with various inclusions such as wood, ceramic, copper and aluminum particles, and carbon fibers. Pejkowski et al. [44] investigated the elastic modulus of plain, carbon-fiber-reinforced and glass-bubbles-reinforced 3D-printed PA using tensile tests. Sola et al. [45] reviewed and compared existing tensile testing standards using PLA samples with different fill angles. Another method of determining the elastic modulus is to measure the natural frequency of a sample. Medel et al. [46] used this approach for a non-contact measurement using a scanning laser vibrometer and an electrodynamic shaker. They found significant influences of the fill angle, print orientation and nozzle temperature on the elastic modulus of PLA. Pszczołkowski et al. [47] compared the measured elastic modulus of PLA and ABS samples varying the nozzle temperature using a tensile test and two nondestructive techniques: the impulse-excitation technique and the ultrasonic method. They concluded that the nondestructive methods measured an elastic modulus that was approximately 1 GPa (50%) higher than with the tensile test.

To characterize the damping of 3D-printed structures, researchers use various modal analysis techniques. He et al. [48] studied the effects of nozzle size, fill ratio, and fill pattern on the damping of ABS using the logarithmic descent method. A similar approach using a curve-fit method to calculate the damping was used by Öteyaka et al. [49] to investigate the effects of fill ratio and fill pattern on the damping properties of PLA. Medel et al. [50] used a non-contact measurement of damping of the PLA with an electrodynamic shaker and a scanning laser vibrometer. They used the half-power method to calculate the damping to study the effects of print orientation, nozzle temperature, and print speed. Another method for characterizing damping is dynamic mechanical analysis (DMA). Morettini et al. [51] and Wang et al. [52] used it to analyze the effects of print orientation, layer height, fill rate, and nozzle temperature on the damping properties of PLA.

The most common method of measuring CTE is a thermomechanical analysis (TMA). For example, Bute et al. [53] used it to investigate the effect of print orientation on the CTE of various thermoplastics and their composites. Qahtani et al. [54] also used TMA to investigate the effects of biobased poly inclusions in PLA on CTE. TMA was also used by Faust et al. [55] to measure the CTE of PA and carbon-fiber-reinforced PA samples with different print orientations and fill angles. The alternative non-contact method for measuring thermal deformation is digital image correlation (DIC). Chen et al. [56] used DIC with non-contact temperature measurements with a thermal camera to measure the CTE of a carbon-fiber-reinforced PA metamaterial unit cell. Similarly, Momenzadeh et al. [57] used DIC and a thermocouple for temperature to study the CTE of polyvinylidene fluoride (PVDF) and its composite with zirconium tungstate powder. Another method for measuring thermal deformation is to use fiber Bragg-grating sensors. Kousiatza et al. [58] used it in combination with a thermocouple to study the CTE of carbon- and glass-continuous-fiber-reinforced thermoplastic composites. CTE can also be measured with a dilatometer. Arif et al. [40] used this method to study the effects of carbon nanotubes and graphene nanoplatelets on the CTE of polyether ether ketone (PEEK).

While the elastic modulus, damping and CTE are usually identified separately, they can also be researched at the same time. Morettini et al. [51] and Wang et al. [52] researched the elastic modulus and damping of PLA using tensile tests and DMA, respectively. Similarly, Vidakis et al. [59] used a tensile test for the elastic modulus and DMA for the damping identification of polypropylene/alumina nanocomposites. Medel et al. [50] simultaneously identified the elastic modulus and damping of PLA; the measured dynamic response of a sample was used

to identify the elastic modulus from the first two natural frequencies and the damping using the half-power method. Chapman et al. [60] used the combination of a tensile test for the elastic modulus and TMA for the CTE to research PA. Similarly, Dul et al. [61] investigated ABS and ABS with the addition of 4 wt% graphene nanoplatelets, and Moreno-Sánchez et al. [62] investigated ASA and ASA reinforced with basalt fibers. Fros and Vesely [63] identified the elastic modulus, damping and CTE of carbon nanotubes and graphene-nanoplatelets-reinforced PEEK. A tensile test was used to measure the elastic modulus, TMA for CTE and DMA for damping. Arif et al. [40] examined the effect of carbon black on PETG and PLA using a tensile test for the elastic modulus, dilatometer for CTE and DMA for damping measurements.

This research introduces a method for the simultaneous and non-contact identification of temperature-dependent elastic modulus, damping, and CTE. The non-contact identification is based on two optical systems (optical camera and thermal camera), a scanning laser vibrometer, IR heating and electrodynamic shaker excitation. The temperature-dependent elastic modulus' identification is based on the natural frequency of the cantilever beam; the temperature-dependent damping identification is based on the circle fit method; and CTE is based on the DIC method and the spatial temperature information from the thermal camera. The proposed sample design makes it possible to research multiple 3D-printing parameters (e.g., fill angle, print orientation, fill density and print speed) on the elastic modulus, damping, and CTE. Based on the proposed method, the 3D prints and the materials used for 3D printing can be characterized for the development of 3D-printed electrothermal soft actuators.

The manuscript is structured as follows. In Section 2 the theoretical background of the methods used is presented. In Section 3, the method for simultaneous, non-contact identification of the temperature-dependent elastic modulus, damping and coefficient of thermal expansion in 3D-printed structures is introduced. The application of the introduced method to various thermoplastics is given in Section 4. Section 5 gives the results and discussion. Finally, conclusions are drawn in Section 6.

2. Theoretical background

Thermoplastic-extrusion 3D printing involves building the parts layer by layer from the bottom up by heating and extruding a thermoplastic filament [64]. Due to the manufacturing process, the mechanical properties of the structures depend on various parameters, which can be divided into two groups: manufacturing and structural parameters [65]. The manufacturing group includes, for example, extrusion temperature, print speed, print-bed temperature and ambient temperature. The structural group includes, for example, the distance between the material decomposition lines, the layer height, the orientation of the printed part and the fill angle.

For structures with material decomposition in a single direction, as shown in Fig. 1, the material properties are assumed to be symmetric in 3 orthogonal planes (along the deposited material and transversely in the horizontal and vertical planes), resulting in orthotropic material properties [66]. This article focuses on the identification of the elastic modulus, damping and CTE in the principal directions, with the 1st principal axis pointing in the direction of the material decomposition lines, the 2nd perpendicular to them, and the 3rd orthogonal to the layers, see Fig. 1.

2.1. Elastic modulus

When a solid behaves in a linearly elastic way, the stresses are proportional to the strains with a factor of the elastic modulus, as described by Hooke's law [67]. In addition to the classical tensile test, the elastic modulus can also be measured using dynamic, non-destructive methods [46,47]. From the dynamic response of a beam,

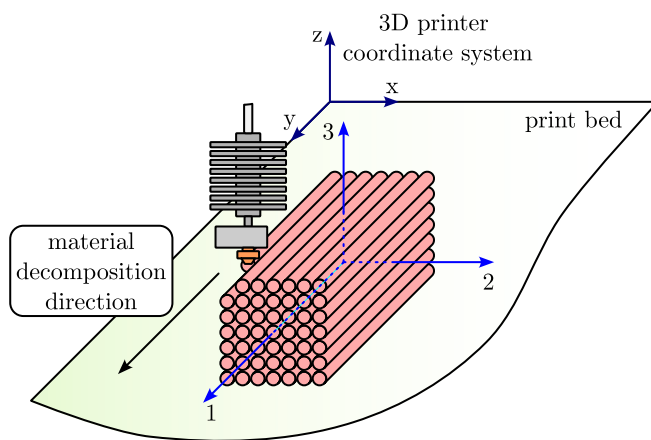


Fig. 1. Unidirectional 3D-printed structure with principal coordinate system.

the elastic modulus can be calculated using the Euler–Bernoulli theory of the free lateral vibration of the beam as [68]:

$$E = \frac{4\pi^2}{(\beta_n l)^4} \frac{f_n^2 \rho A l^4}{I}, \quad (1)$$

where $\beta_n l$ is the dimensionless constant of the n th natural frequency that depends on the boundary conditions of the beam, f_n is the n th natural frequency, ρ is the material density, A is the cross-sectional area, l is the beam length, and I is the area moment of inertia. The value of $\beta_1 l$ for the 1st natural frequency of a fixed-free (cantilever) beam is known to be $\beta_1 l = 1.875104$ [68].

2.2. Damping

Damping refers to the dissipation of energy in a system, typically through the conversion of mechanical energy to heat [68]. The damping ratio δ is a dimensionless parameter used to describe the damping in a structure. It is defined as the ratio of the damping force to the critical damping force of a structure [68]. Here, the circle-fit method for the damping identification will be briefly introduced. For more details, the reader is referred to the work of He and Fu [69].

The method is based on the circular shape of the frequency-response function (FRF) of a Nyquist plot. The FRF is defined as the ratio between the Fourier transform of the response (displacement) and the excitation (force) [69]. The FRF is a complex function of the frequency, and when shown as a Nyquist plot near the resonant frequency it forms a circle. The damping ratio is identified from the circle fit. First, the natural frequency (ω_r) is determined as the frequency at the point with the maximum arc change [69]. Once the natural frequency is known, the damping ratio can be estimated using any two FRF points before and after ω_r as [69]:

$$\delta = \frac{\omega_a^2 - \omega_b^2}{2\omega_r^2} \frac{1}{\tan(\theta_a/2) + \tan(\theta_b/2)}, \quad (2)$$

where ω_a and ω_b are the frequencies after and before ω_r , respectively, and θ is the angle between the selected point and ω_r is measured from the center of a circle.

2.3. Coefficient of thermal expansion

The coefficient of thermal expansion (CTE) is a parameter that expresses the fractional change in length per unit temperature change [70]. In general, CTE depends on the temperature, but in a certain temperature range where the length varies linearly with temperature, it can be treated as a constant. CTE is defined as [70]:

$$\alpha = \frac{1}{L_0} \frac{\Delta L}{\Delta T} = \frac{\epsilon}{\Delta T}, \quad (3)$$

where L_0 is the initial length, ΔL is the change in length due to the change in temperature ΔT . The fractional change in length $\Delta L/L_0$ is the thermal deformation described by the engineering strain $\epsilon = \Delta L/L_0$ [71].

2.4. Digital image correlation

Digital image correlation (DIC) is a non-contact optical technique for measuring strain and displacement [72]. DIC tracks the displacement and deformation of a square subset of pixels in an image called a region of interest (ROI). To find a unique displacement and deformation, it is important that the ROI has a random pattern that is diverse in contrast and intensity level. The goal is to find the mapping function between the ROI in the reference image and the current image [73]. If an affine transformation is used as the mapping function, planar displacements and deformations can be found. Mathematically, the problem is formulated as a multivariable optimization problem [73]. The zero-mean normalized sum of the squared difference is usually chosen as the cost function, using the Newton–Raphson method to resolve the transformation parameters [74]. For more accurate results not limited by pixel resolution, ROI is interpolated and subpixel accuracy is achieved [75].

2.5. Glass-transition temperature

The glass-transition temperature, represented by T_g , marks the point at which the amorphous regions of a polymer transition from a stiff, rigid state to a more flexible, rubbery state [76]. This transition in the mobility of the polymer chains is also referred to as the alpha transition T_α , especially in dynamic applications [77]. This temperature marks the boundary between the solid and the rubbery state of the material. It is a property of amorphous materials and the amorphous portion of semi-crystalline materials. The T_g of a material can vary depending on its molecular structure, with materials having a flexible backbone exhibiting a lower T_g and materials having a stiff, rigid, and inflexible structure exhibiting a higher T_g . One way to determine T_g is to look at the decrease in elastic modulus with temperature as the transition from a rigid state to a rubbery state occurs [77].

3. Simultaneous non-contact identification of the elastic modulus, damping and coefficient of thermal expansion in 3D-printed structures

3.1. Sample geometry

The proposed sample, named 3T, is shown in Fig. 2. The 3T sample is a symmetric 6-cantilevered beam structure; the beams have three different lengths (L_0 , L_1 , and L_2). The number of beams and their lengths can be adjusted to meet the requirements of the experiment. This design allows 6 simultaneous measurements of the elastic modulus, damping and CTE. The thickness t and the width w of the beams can be varied to contain a sufficient number of material deposition lines for a representative sample of the 3D-printed structure, while keeping t small to minimize the temperature gradient. The beams on the same side are separated by distance g_1 and by a notch g_2 with a depth equal to the beam thickness (t). The notch is important to separate the natural frequencies identified later. The 3T sample is fixed to the electrodynamic shaker via the base of width b_w and height b_h .

The main advantage of the proposed 3T sample is that each beam can be 3D printed with different parameters. This allows the study of different effects of the 3D-printing parameters on the material properties within a single sample. In this research different lengths are used to research the effect of natural frequency on the elastic modulus and to cover large differences in the elastic modulus (e.g., PETG vs. TPU).

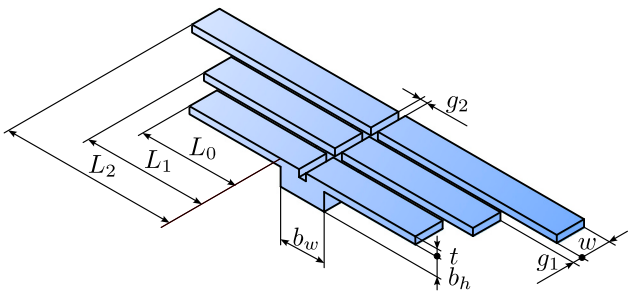


Fig. 2. The 3T sample geometry.

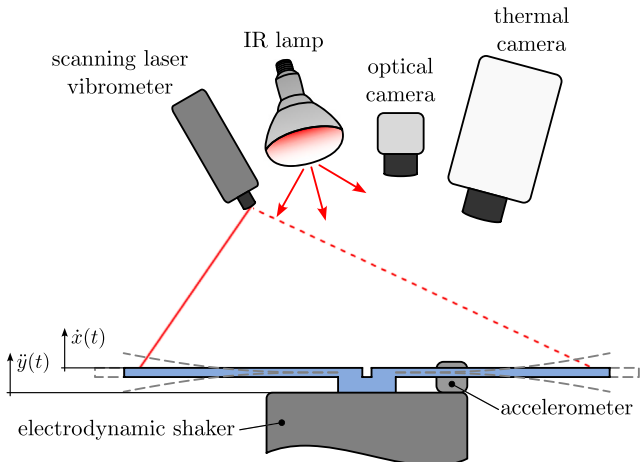


Fig. 3. Method experiment setup.

3.2. Method experiment setup

The experimental setup of the introduced method is shown in Fig. 3. The 3T sample is mounted on the electrodynamic shaker and subjected to a relatively small amplitude of vibrations. Small vibrations are used to excite the natural dynamics of the sample and not affect the in-plane deformation. The 3T sample is uniformly heated to the desired maximum temperature using the IR lamps (non-contact). To further enhance the heating of the 3T sample, the IR-reflective surface is placed behind the 3T sample and the sample's back side is painted black with a temperature paint. After heating, the 3T sample is cooled to the desired minimum temperature by convection, releasing the heat to the surroundings ($22\text{ }^{\circ}\text{C}$). During the temperature cycle, images are captured simultaneously by two cameras, one for the visual spectrum and one for the IR spectrum. The dynamic response of each beam of the 3T sample is also measured with a scanning laser vibrometer and the excitation of the electrodynamic shaker with an accelerometer. The 3T sample can be heated and cooled for the desired number of temperature cycles. The experiment ends with the glass transition step: the 3T sample is heated to a temperature above T_g and the measurements are stopped when excessive deformation occurs.

3.3. Identification of elastic modulus

The scanning laser vibrometer and electrodynamic shaker are used for non-contact identification of the elastic modulus based on the natural frequency of a beam on a 3T sample. Eq. (1) is used to determine the elastic modulus. The linear dimensions of the 3T sample are measured to determine the length L , cross-section area $A = w \cdot t$, and area moment of inertia $I = w \cdot t^3/12$ of a beam (Fig. 2). From the measurements the volume of a whole 3T sample is calculated (see Appendix A) to determine the material density ρ from the measured mass. The first

natural frequency f_1 is estimated from the first peak on the magnitude plot of the FRF and then exactly identified with the circle-fit method. In this way the elastic modulus is determined in the direction of the principal axis running along the length of the beam (Fig. 1).

To study the effect of temperature on the elastic modulus during the temperature cycling the dynamic response of the beams is measured at regular temperature intervals. The temperature of the measured elastic modulus is determined using the temperature of the beam based on the thermal camera image taken during the response measurement. Due to the potential temperature gradient along the length of a beam, only a specific region of the beam is considered when evaluating the temperature. The region is near the fixed support where the maximum stress in the first mode shape is expected to occur, since the change in material properties due to temperature in this region has the greatest effect on beam stiffness. For details see Appendix B.

3.4. Identification of damping

Based on the scanning laser vibrometer's response and the electrodynamic shaker base excitation the damping ratio is identified using the circle-fit method. The damping ratio is estimated simultaneously with the natural frequency using Eq. (2). The damping ratio of the beam in the direction of the principal axis running along the length of the beam (Fig. 1) is estimated at different temperatures to investigate the temperature dependence. The temperature of the measured damping ratio is determined in the same way as for the elastic modulus.

3.5. Identification of coefficient of thermal expansion

The optical camera and thermal camera in combination with IR heating are used for a non-contact identification of the CTE from a series of simultaneous images taken during temperature cycling.

DIC is used to calculate the deformation of the 3T sample beam due to temperature changes from the optical camera images. The deformation of the beam is calculated using the ROI, where the beam is free to thermally deform. Therefore, to avoid the boundary effects, the ROI should have a certain distance from the fixed support. The deformation ϵ is calculated in the directions along and perpendicular to the beam length, which allows for the identification of CTE in two directions from one beam.

The temperature change of a beam is calculated from the thermal camera images. First, the temperature is evaluated from the thermal camera image within the same region of the beam that was used for the DIC. Then, the temperature change ΔT is calculated as the temperature difference between the current image and the reference image.

With known deformation ϵ and temperature change ΔT , CTE is determined using linear regression in the temperature window where the linear trend is observed, according to Eq. (3). In this way, CTE in the direction of the principal axis running along and perpendicular to the length of the beam (Fig. 1) is determined from the corresponding deformation.

4. Experimental research

4.1. 3D printing of 3T samples

The introduced method was used to investigate the effects of print orientation and fill angle on the elastic modulus, damping, and CTE of 3D-printed structures made of 9 different materials, see Table 1. Composite materials tested include PLA with added wood particles (woodPLA), PLA with added stone powder (stonePLA), PA with added carbon fibers (PACF), and PA with added glass fibers (PAGF). In addition, TPU with a high thermal conductivity of $6\text{ W m}^{-1}\text{ K}^{-1}$ (thermalTPU) was tested.

The three most common print orientations were used, i.e., horizontal (H), vertical (V) and lateral (L), in combination with three

Table 1
Researched materials.

Filament	Manufacturer	Referred to as	Print settings			Experiment
			Nozzle Temp. [°C]	Bed Temp. [°C]	Print speed [mm/s]	
Prusament PLA	Prusa Polymers a.s.	PLA	215	60	30	50
EasyWood Cedar	Formfutura VOF	woodPLA	220	60	30	55
StoneFil Terracotta	Formfutura VOF	stonePLA	228	60	30	55
Prusament PETG	Prusa Polymers a.s.	PETG	250	85	30	70
TPU filament	PLASTIKA TRČEK d.o.o.	TPU	230	60	15	60
Ice9 Insulating	TCPoly, Inc.	thermalTPU	230	60	15	60
PA6 Low Warp	Spectrum Group Sp. z o.o.	PA	260	90	30	70
NYLON PA12+CF	Fiberlab S.A.	PACF	260	90	30	70
NYLON PA12+GF15	Fiberlab S.A.	PAGF	260	90	30	70

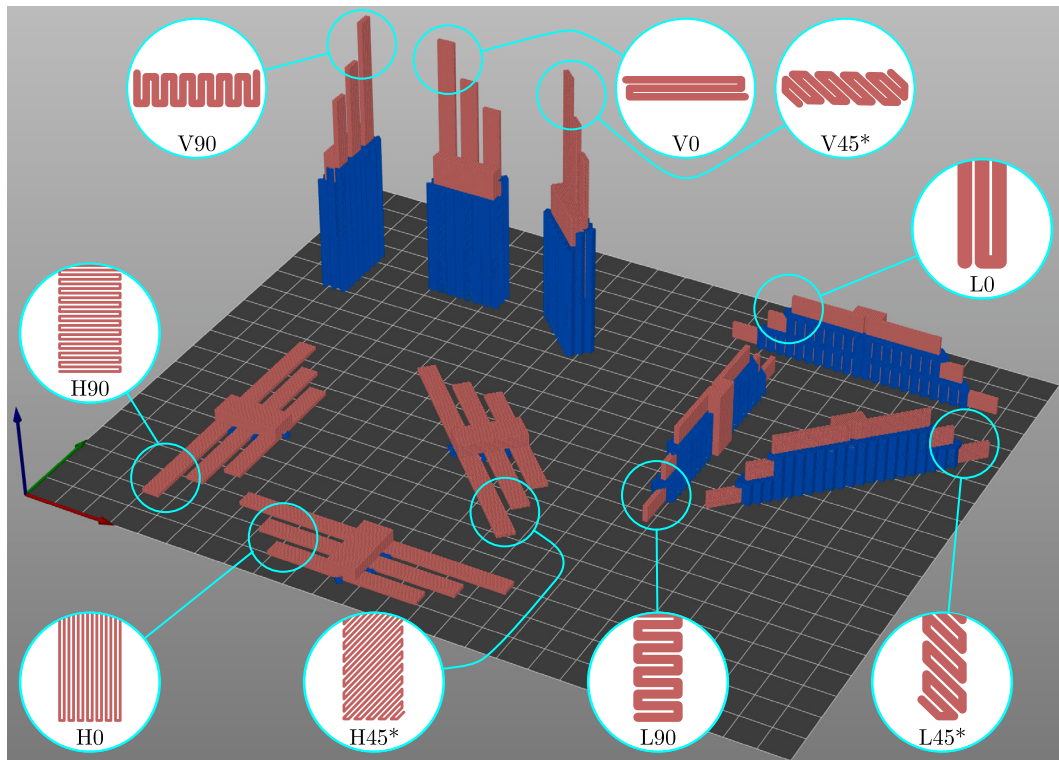


Fig. 4. Researched parameters of 3D printing, details not to scale.

different fill angles, i.e., 0° (denoted as: 0), 90° (90), and alternating 45°/−45° (45*), as shown in Fig. 4. This results in a total of 81 printed 3T samples. They were named based on the material name, print orientation and fill angle, e.g. PLA H0 refers to a 3T sample that was 3D printed with Prusament PLA material in a horizontal orientation with a fill angle of 0°.

All the 3T samples were printed on an E3D Toolchanger to utilize multi-material printing for supports. They were printed with a 0.4-mm nozzle and 0.45-mm extrusion width, 0.2-mm layer height and 100% fill density. Other filament-specific settings are shown under Print Settings in Table 1. The 3D-printing process took approximately 70 h to fabricate 81 3T sample configurations.

The dimensions of the 3T sample were iteratively improved to obtain a sample suitable for simultaneous measurements of elastic modulus, damping, and CTE. The base width $b_w = 10$ mm and height $b_h = 4$ mm were chosen to allow repeatable attachment to the shaker and sufficient overlap of the beams to model the joint as a fixed support. At the same time, the base must remain small so that it does not act like a heat capacitor and disturb the temperature field. The distances $g_1 = 2$ mm and $g_2 = 1$ mm between the beams were sufficient to limit their interactions during the vibration and separate their natural frequencies (Fig. 2). The beam width $w = 6$ mm and the thickness

$t = 1.8$ mm were chosen to achieve a high surface-area-to-volume ratio for rapid heating and cooling. The beam thickness was chosen to minimize the temperature gradients and keep the beams slender, yet thick enough to contain at least 3 material decomposition lines in all the printing configurations.

The length of the longest beams on the 3T sample $L_1 = 40$ mm was chosen as the maximum that we could still homogeneously heat with the experimental setup. The other two beams were chosen to be shorter to compensate for the drop in natural frequency outside the excitation bandwidth during heating, especially for the flexible materials. In this way the elastic modulus and damping could still be measured from the shorter beams. The length of the shortest beam was chosen to be $L_3 = 20$ mm to keep its slenderness slightly above the limit for the validity of Euler's beam theory ($L/t > 10$ [78]). The length of a middle beam $L_2 = 28$ mm was selected so that the natural frequencies of the beams are reasonably uniformly distributed in the frequency space for all the materials tested. This design allows simultaneous measurements of the elastic modulus, damping and CTE using a single 3T sample with the same geometry for all the materials tested.

Due to the nature of the thermoplastic-extrusion 3D printing, the structures consist of a discrete number of material-deposition lines. For this reason, the dimensions of the final structures do not always match

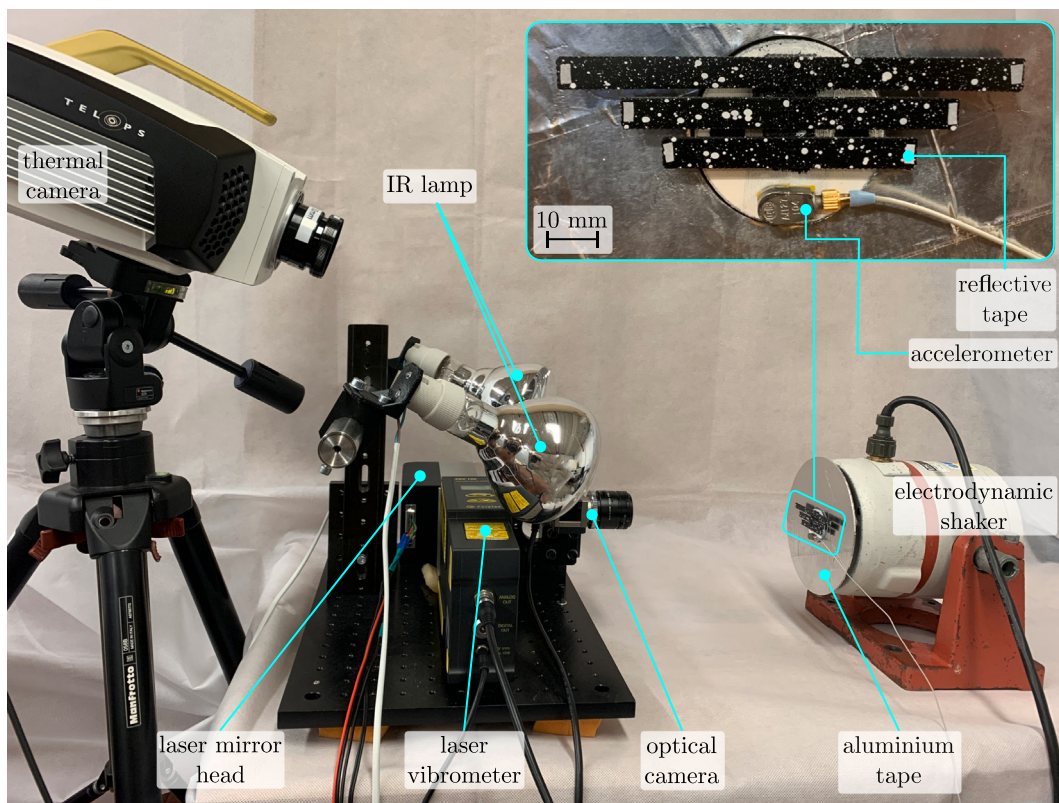


Fig. 5. Experimental setup.

Table 2
The 3T samples dimensions.

Dimension	3T sample			
	H45*, L45*, V45*	H0, V90	L0, V0	H90, L90
L_1 [mm]	40	40	40	40.01
L_2 [mm]	28	28	28	28.20
L_3 [mm]	20	20	20	20.06
w [mm]	6	6.15	6	6
t [mm]	1.8	1.8	1.67	1.8
b_w [mm]	10	10	10	9.81
b_h [mm]	4	4	4.11	4

the desired dimensions. In order to obtain a symmetrical 3T sample the dimensions perpendicular to the material-decomposition lines were chosen to be a multiple of the line width, with the spacing also taken into account. Similarly, the dimensions in the direction of the z axis of a 3D printer were chosen to be a multiple of the layer height. This results in different dimensions of the 3T samples depending on the print orientation and fill angle, as shown in Table 2.

4.2. Experimental setup

Fig. 5 shows the experimental setup of the introduced method. After the 3T sample was printed, its dimensions were measured with a caliper. Then the 3T sample was weighed using the EMB 200-3 (KERN) weight (accuracy of 0.001 g). The top and bottom of the 3T specimen were first painted with matte black paint spray, then a random speckle pattern was applied to the top with matte white paint spray. The 3T sample was superglued to the electrodynamic shaker head. The electrodynamic shaker LDS V406 (Brüel & Kjaer) was used together with the amplifier EP4000 (Behringer) to excite the 3T samples with white noise in the frequency range 30–2000 Hz generated by an NI 9263 (National Instruments Corporation) measurement card.

An A/127/V (DJB Instruments) accelerometer with a temperature range from -50 to 125 °C was mounted on the electrodynamic shaker head under the 3T sample to monitor the excitation. The velocity response of each beam was measured using a PVD 100 (Polytec) laser vibrometer with a custom mirror head adapter to automatically position the laser beam to a measurement point at the end of each beam. Reflective tape was used to amplify the laser signal. An NI 9234 measurement card was used to acquire the signals from the accelerometer and laser vibrometer. The excitation and response signals were measured sequentially for 1 s at each beam throughout the experiment.

Two 150-W IR lamps were used to achieve uniform heating of the 3T sample. A surface covered with aluminum tape was placed behind the 3T sample to reflect the IR light and promote heating from behind as well. Images during the temperature cycles were simultaneously acquired using the acA4112-20um (Basler ace) optical camera and the FAST M3k (Telops) thermal camera. Not to interfere with the thermal camera, the IR lights were turned off during image acquisition. Both cameras used the same trigger signal generated by an NI 9263. The triggering of the image acquisition was controlled to have a constant temperature resolution of ~ 0.5 °C. The 3T sample was heated and cooled for 3 temperature cycles between the minimum (T_{\min}) and maximum (T_{\max}) temperatures. The heating and cooling rates exhibited variability across materials attributed to variations in thermal diffusivity (for further information, refer to Appendix C). On average, the heating rate was 5.8 °C/min, while the cooling rate was -8.9 °C/min. The minimum temperature was chosen to be $T_{\min} = 30$ °C, because this temperature was reached relatively quickly at room temperature (22 °C). The maximum temperature was unique for each material tested, as it must be lower than its T_g , and is given under Experiment in Table 1. After completion of the third temperature cycle, the glass transition step was performed: the 3T sample was heated to the maximum temperature ~ 90 °C and if excessive deformation occurred beforehand, the measurement was stopped.

The experiment for a single 3T sample lasted about 40 min, resulting in roughly 50 h of experimental data. Optical and thermal cameras each

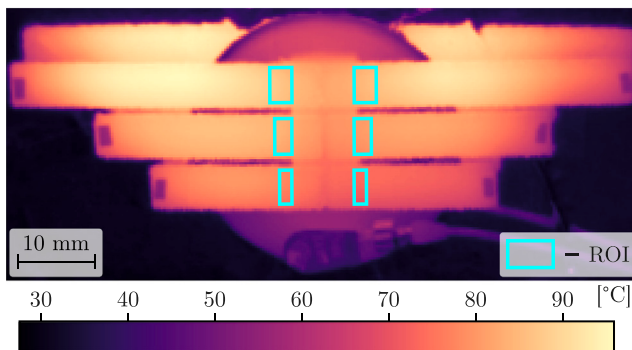


Fig. 6. ROIs on the thermal camera image of each beam on the 3T sample used to calculate the temperature at which the elastic modulus was identified.

Table 3

Mapping from the print orientation and fill angle of a 3T sample to a principal direction in which the elastic modulus and damping ratio are identified.

	Print Orientation	Fill Angle		
		0	90	45*
H		1	2	*
L		1	2	*
V		3	3	3

captured around 460 images, and the dynamic responses of each beam and excitation were measured approximately 150 times per sample. Evaluating the data for a single 3T sample took about 45 min.

4.3. Identification of the elastic modulus

Eq. (1) was used to identify the elastic modulus. The cross-sectional areas A , the area moments of inertia I , and the lengths L of the beams, as well as the material density ρ , were determined by caliper and weight measurements. They were considered constant at all the tested temperatures. Their change due to thermal expansion had no significant effect on the calculated elastic modulus, compared to the effect of the change in natural frequency with the temperature.

The first natural frequency f_1 of each beam on the 3T sample was determined at a given temperature using the circle-fit method. To fit the circle to the frequency-transfer function between the velocity of the beam and the electrodynamic shaker acceleration, 15 frequency points were selected both before and after the assumed natural frequency. Then, the exact first natural frequency was identified as the frequency of the point of maximum arc change, as described in Section 2.2. The range of the determined natural frequencies for each material is shown in D.

The temperature of the identified elastic modulus was determined for each beam as the average temperature within the ROI near its fixed support from the images taken by the thermal camera during its individual dynamic-response measurement, as shown in Fig. 6. The ROI extends from the edge of a base (beginning of a fixed support) to 7% of a beam length to include the ROI where the stress in the first mode shape is higher than 90% of the maximum stress for a cantilever beam (for details, see Appendix B). The ROI is also 1 mm away from both edges of the beam to exclude the boundary effects.

Depending on the print orientation and fill angle of the 3T sample, the elastic modulus in the principal directions was identified, as shown in Table 3. For configurations marked with “*”, the elastic modulus in the principal directions cannot be identified, and instead, the elastic modulus for alternating fill angles was determined.

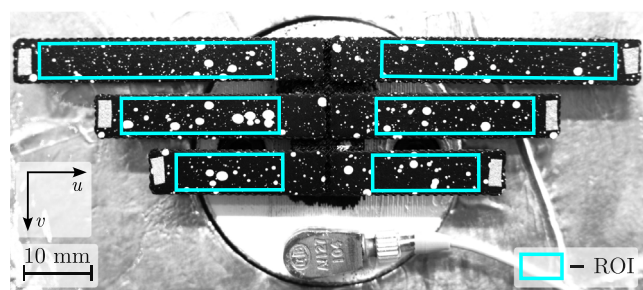


Fig. 7. ROIs in the optical camera image of each beam on the 3T sample used to calculate the deformation.

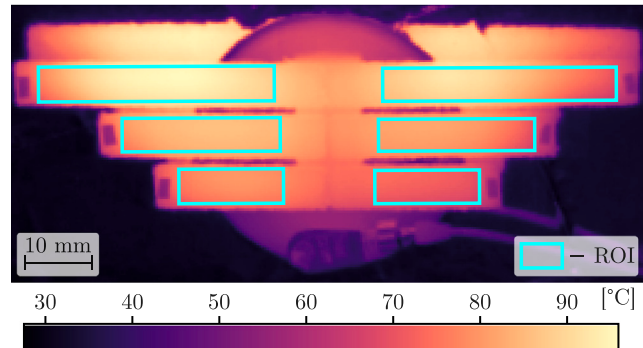


Fig. 8. ROIs in the thermal camera image of each beam on the 3T sample used to calculate the temperature.

4.4. Identification of damping

The identification of the damping was performed simultaneously with the identification of the natural frequency using the circle-fit method. The initial steps of the circle-fit method were the same as described in Section 4.3. With the resonant frequency point in the Nyquist plot known, 4 pairs of frequency points before and after the natural frequency were used to calculate the damping ratio using Eq. (2). The final damping ratio was then calculated as the average of the four. The temperature at which the damping ratio was identified was the same as for the elastic modulus (see Section 4.3). Depending on the print orientation and fill angle of the 3T sample, the damping ratio in the principal directions was identified, as shown in Table 3.

4.5. Identification of the coefficient of thermal expansion

The selected ROI for the DIC analysis on each beam on the 3T sample is shown in the optical camera image, see Fig. 7. The ROI was 7% of the total beam length from the fixed support, starting where the temperature ROI of the elastic modulus ended, to avoid the boundary effect of a fixed support. To exclude the reflective tape at the end of a beam the ROI was 3 mm shorter than the beam length. Also, a distance of 1 mm was used between the ROI and the horizontal edges of the beam to avoid boundary effects. The DIC method was used to identify the deformation in the direction of the beam length (u) and perpendicular to it (v) from the series of acquired images (see Section 2.4).

The temperature of the beam was determined as the average temperature within the ROI from the thermal camera image, as shown in Fig. 8. The ROI includes the same region as the ROI used for DIC.

The heat capacity of the material contributes to a discrepancy between the measured surface temperature and the average temperature within the beam. During the IR lamps' heating phase the surface temperature is slightly higher than the one inside the sample, and vice

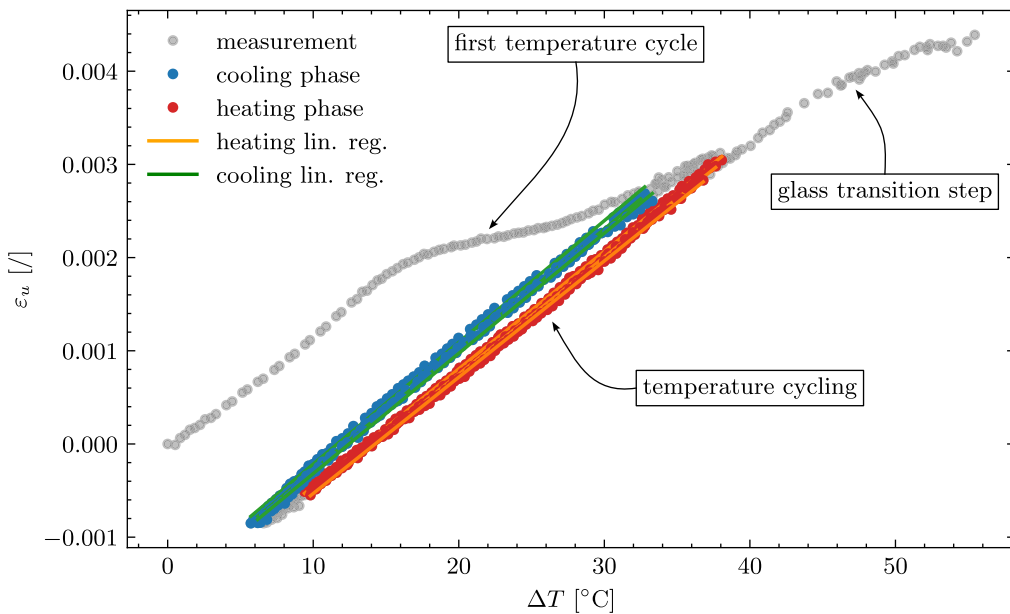


Fig. 9. Deformation vs. temperature change of a beam on a PACF V90 3T sample.

Table 4

Mapping from the print orientation and fill angle of a 3T sample, and deformation direction from DIC to a principal direction in which CTE is identified.

Print orientation	Fill angle	Deformation direction	
		<i>u</i>	<i>v</i>
H	0	1	2
	90	2	1
	45*	*	*
L	0	1	3
	90	2	3
	45*	*	3
P	0	3	1
	90	3	2
	45*	3	*

versa during the convection-cooling phase resulting in a hysteresis. Therefore linear regression was performed separately for the data obtained during the heating and cooling phases, as shown in Fig. 9. To mitigate the nonlinear effects of hysteresis, only measurements with temperatures greater than $T_{\min} + 5$ during heating and less than $T_{\max} - 5$ during cooling were utilized for the linear regression analysis. The final CTE was obtained by calculating the average of the fitted regression coefficients during cooling and heating.

In this way the CTE was identified in the *u* and *v* directions for each beam on the 3T sample (Fig. 7). Depending on the print orientation, fill angle, and deformation direction, CTE in the principal direction was identified according to Table 4. For the configurations marked with “*”, the CTE in the principal directions cannot be identified, and instead, CTE for the alternating fill angles is determined.

4.6. Identification of the glass-transition temperature

The glass-transition temperature was identified from the reduction in the elastic modulus as the temperature increases above T_g . Fig. 10 shows the procedure for identifying T_g . First, the elastic-modulus measurements during the glass-transition step were divided into two groups using data segmentation with the dynamic programming search method and L2 regularization [79]. Linear regression was then applied to both groups, and the point of intersection of the two lines, indicating the decay of the elastic modulus and hence T_g , was determined. This

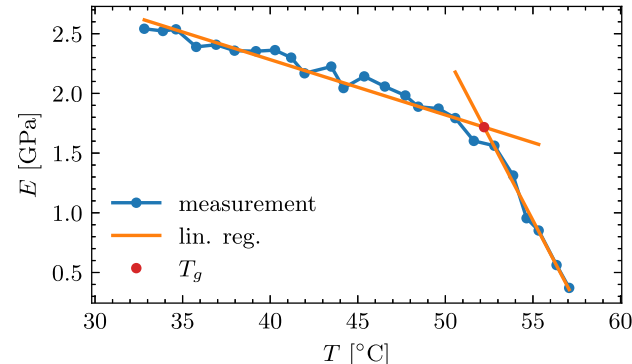


Fig. 10. Identification of glass-transition temperature for a beam on PLA V0 3T sample.

approach was implemented on all the beams of the 3T sample, and an average T_g value was computed.

5. Results and discussion

Fig. 11 shows the measured elastic modulus in the direction of the principal axes and for an alternating fill angle (*) in the observed temperature range. Different beam lengths (natural frequencies) had no significant effect on the calculated elastic modulus, so the continuous function of the elastic modulus as a function of temperature was obtained by averaging the measured elastic moduli of all the beams within the rolling ± 2 °C temperature window. Base materials (PLA, PETG, TPU and PA) show similar elastic moduli in all 3 principal directions and for the alternating fill angle. Therefore, 3D-printed structures with 100% fill of these materials can be modeled as isotropic materials in terms of their elastic properties. However, when inclusions are added, the elastic properties become directional. Composite materials (wood-PLA, stonePLA, thermalTPU, PACF and PAGF) have the highest elastic modulus in the direction of the 1st principal axis and the lowest in the direction of the 3rd principal axis. During extrusion of the material, the inclusions tend to align in the direction of flow and solidify during deposition. Hence, the highest stiffness in the 1st principal direction. The structures are less stiff in the direction perpendicular to the inclusions (2nd principal axis) and even less orthogonal to them (3rd principal

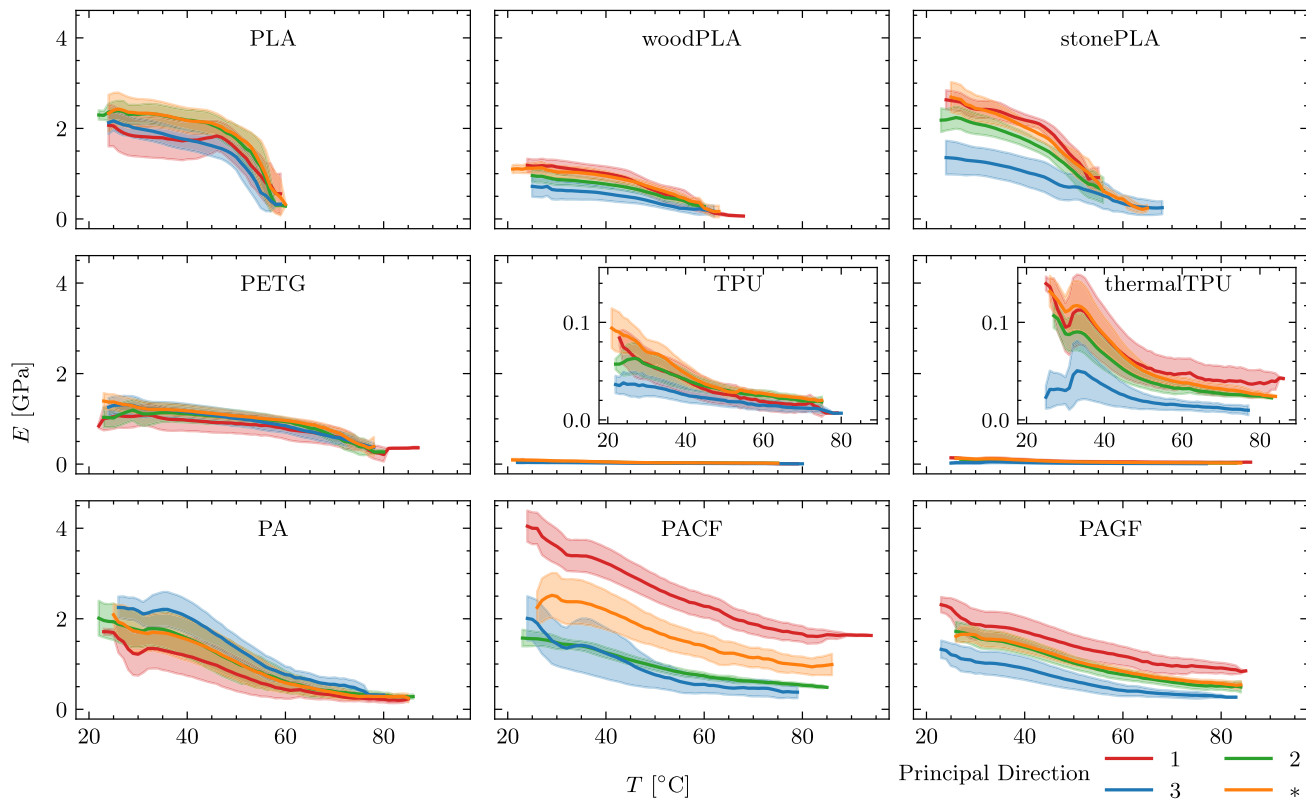


Fig. 11. Principal elastic moduli and elastic modulus of alternating fill (*) as a function of temperature.

axis), where most of the load is carried by the matrix. As expected, the elastic modulus of the alternating fill angle is between the 1st and 2nd principal elastic modulus. All of the materials studied show a linear decrease in the elastic modulus with a temperature in the observed temperature range. Some of the less thermally stable materials show a significant drop in elastic modulus at T_g , which we will discuss later.

The measured damping ratio in the observed temperature range is shown in Fig. 12. It was found that the damping ratio has no significant dependence on the print orientation and fill angle. Therefore, an isotropic damping model can be used for 3D-printed structures with 100% fill made of these materials. TPU and thermalTPU exhibited a higher damping ratio as they were in a rubbery state in the temperature range of the measurement. Other materials exhibited a similar damping ratio at low temperatures, which then steadily increased with temperature. The damping ratio of PLA and PETG is the least affected by temperature, up to a peak. The peak in the damping is also observed for woodPLA and stonePLA. The glass-transition temperature can also be determined as the temperature at maximum peak of damping. However, in the specific case of PLA, the peak associated with the glass transition is not well-defined, and multiple peaks can be observed for woodPLA and stonePLA. This poses a limitation to the aforementioned method's effectiveness. Nonetheless, it should be noted that the maximum peaks of damping (including PETG) occur at higher temperatures than T_g determined by the decrease in elastic modulus (discussed later, refer to Fig. 14). The results also show that the damping ratio increases with the added inclusions only in the case of a PLA matrix.

Fig. 13 shows the measured CTE in the direction of the principal axes and for an alternating fill angle (*) in the temperature range from 30 °C to their T_{max} . Again, the base materials (PLA, PETG, TPU and PA) show similar CTEs in all 3 principal direction and for the alternating fill angle. Therefore, 3D-printed structures with 100% fill from the base materials can be modeled as isotropic materials with respect to CTE. However, when inclusions are added, CTE becomes direction dependent. Composite materials (woodPLA, stonePLA, thermalTPU, PACF

and PAGF) exhibit the largest CTE along the 3rd principal axis, and the lowest CTE along the 1st principal axis. This phenomenon occurs because the inclusions in these materials restrict thermal expansion of the structure, resulting in a lower CTE along the inclusions orientation (the 1st principal axis). Conversely, the structures experience less constraint perpendicular to the inclusions (the 2nd principal axis), and even less orthogonal to the inclusions (the 3rd principal axis), leading to higher CTEs in these directions. As expected, the CTE for the alternating fill angle is between the 1st and 2nd principal CTE.

Up to 90 °C PLA, woodPLA, stonePLA and PETG exhibited the glass transition, see Fig. 14. As expected PETG shows a higher T_g than PLA. The wood and stone inclusions have no significant effect on the T_g of PLA.

6. Conclusions

This research introduces a method for the simultaneous and non-contact identification of temperature-dependent elastic modulus, damping, and CTE. The non-contact identification is based on two optical systems (optical camera and thermal camera), a scanning laser vibrometer, IR heating and electrodynamic shaker excitation. The temperature-dependent elastic modulus identification is based on the natural frequency of the cantilever beam; the temperature-dependent damping identification is based on the circle-fit method; and CTE is based on the DIC method and the spatial temperature information from the thermal camera.

The main advantage of introduced non-contact method over conventional methods is the ability to simultaneously measure elastic modulus, damping, and CTE. In particular, when compared to DMA, which requires separate tests, the proposed method stands out by enabling a comprehensive characterization of these properties in a single test. Additionally, the proposed method utilizes a 3T sample, which allows for the concurrent examination of multiple manufacturing parameters. This means that different beams can be printed at varying speeds, fill

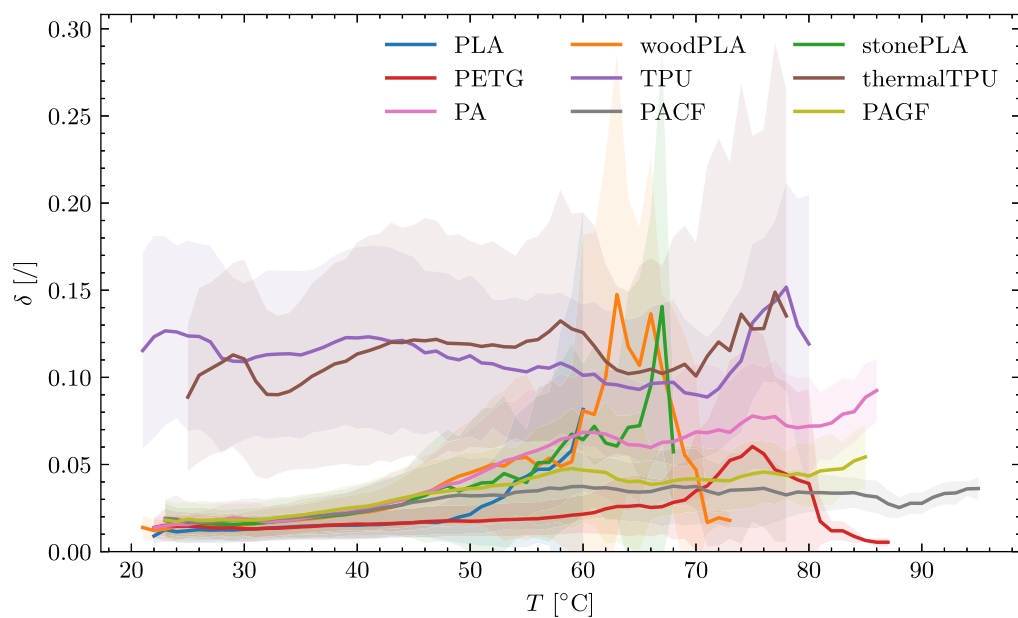


Fig. 12. Damping factor as a function of temperature.

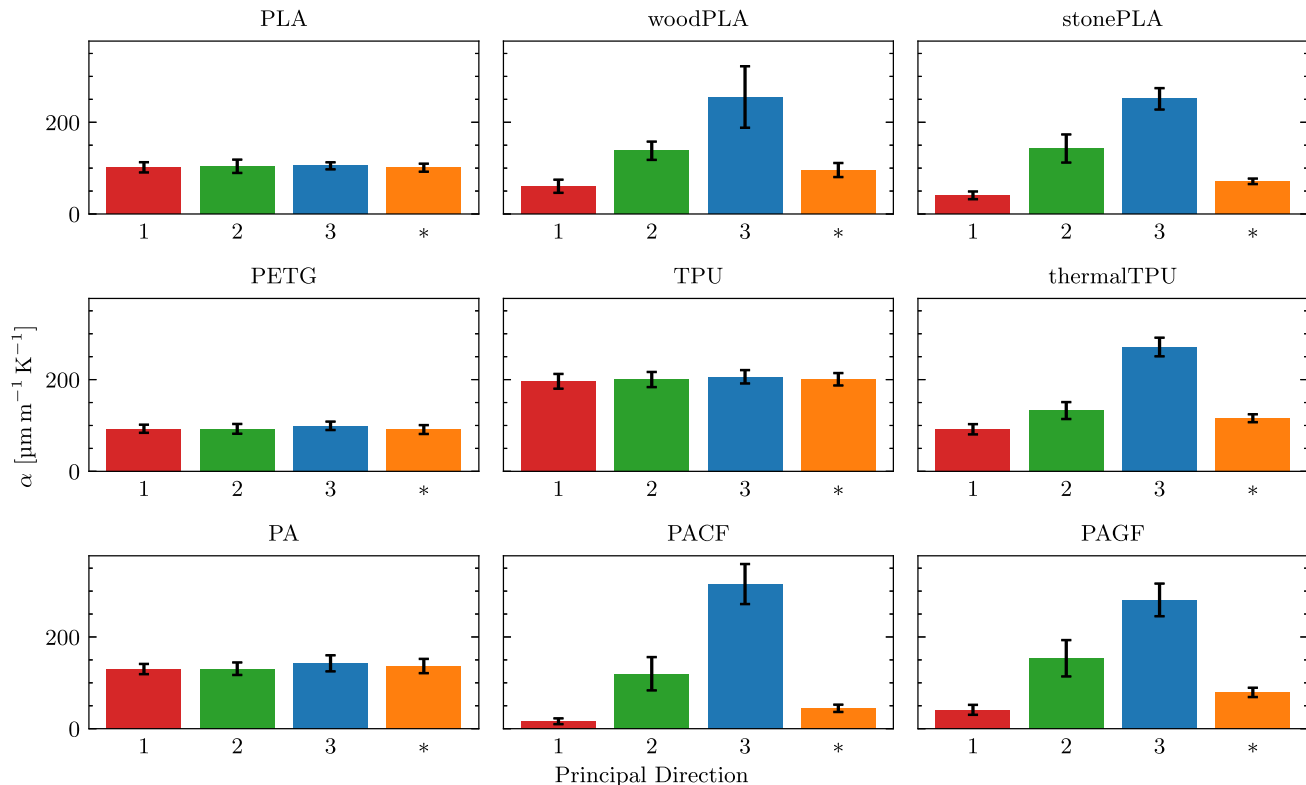


Fig. 13. Principal CTE and CTE of alternating fill (*).

angles or fill rates, allowing for the study of their respective effects within a single experiment. In contrast, DMA requires multiple samples and tests to achieve similar outcomes. Furthermore, DMA measurements are typically limited in terms of frequency and temperature ranges. Such limitations can result in an incomplete understanding of a material's dynamic behavior, as the available frequency range might not encompass the complete spectrum, and the temperature range might fail to capture all relevant thermal transitions or operating conditions of the polymer. In contrast, the proposed method can be expanded to capture material dynamics across extreme temperatures

and frequencies without relying on the time–temperature superposition principle.

In this research the introduced method was applied to investigate the influence of three predominant print orientations and three distinct fill angles on a set of nine materials, including the most common base materials (PLA, PETG, TPU, and PA) and composite materials (woodPLA, stonePLA, thermalTPU, PACF, and PAGF). This resulted in the examination of a total of 81 3T samples.

The results show an isotropic elastic modulus and CTE for the 3D-printed structures of base materials and orthotropic for composite

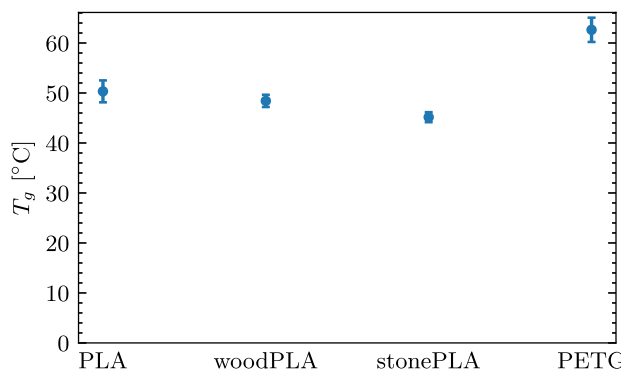


Fig. 14. Glass-transition temperature.

materials. For composite materials the elastic modulus was found to be highest and CTE was found to be lowest in the direction of material decomposition (1st principal axis). Conversely, in the direction of layers (3rd principal axis), the elastic modulus was found to be lowest and the CTE was found to be highest. For structures with alternating infill, the elastic modulus and CTE were found to be between those of the 1st and 2nd principal axes. Additionally, the elastic modulus was observed to decrease linearly with temperature, with a significant drop for materials that exhibit a glass transition.

The damping ratio was found to be isotropic for all the studied materials. Structures of materials below T_g have similar damping ratio at room temperature, which increases with temperature to a maximum at T_g . The materials in rubbery state (TPU and thermalTPU) have a higher damping ratio, showing minimal temperature dependence.

The glass-transition temperature was determined for the PETG, PLA, woodPLA, and stonePLA materials. Added inclusions showed no impact on the glass-transition temperature of materials with a PLA matrix.

CRediT authorship contribution statement

Gašper Krivic: Conceptualization, Data curation, Formal analysis, Investigation, Methodology, Software, Validation, Visualization, Writing – original draft, Writing – review & editing. **Janko Slavič:** Conceptualization, Data curation, Formal analysis, Funding acquisition, Investigation, Methodology, Project administration, Resources, Supervision, Validation, Visualization, Writing – original draft, Writing – review & editing.

Declaration of competing interest

The authors declare that they have no known competing financial interests or personal relationships that could have appeared to influence the work reported in this paper.

Data availability

Data will be made available on request

Acknowledgments

The authors acknowledge the partial financial support from the Slovenian Research Agency, Republic of Slovenia (research core funding No. P2-0263 and research project J2-3045).

Appendix A. Sample volume

The volume of the 3T sample is obtained from the linear dimensions shown in Fig. 2. Firstly, the volume of beams is calculated for a sample with n beams:

$$V_{\text{beams}} = 2 \sum_i^n w t L_i. \quad (4)$$

Secondly, the volume of the base is calculated as:

$$V_{\text{base}} = b_w b_h L_{\text{base}}, \quad (5)$$

where L_{base} is calculated as:

$$L_{\text{base}} = w n + g_1(n - 1). \quad (6)$$

Thirdly, the volume of the beams' overlap on the base is calculated:

$$V_{\text{overlap}} = w(b_w - g_2)t n. \quad (7)$$

Finally, the volume of the sample is calculated:

$$V = V_{\text{beams}} + V_{\text{base}} + V_{\text{overlap}}. \quad (8)$$

Appendix B. Stress distribution in the first mode shape of a cantilever beam

The first natural frequency is associated with the first mode shape. For lateral vibration of a cantilever beam, the first mode shape is defined as [68]:

$$W_1(x) = C_1 [\sin(\beta_1 x) - \sinh(\beta_1 x) - \alpha_1(\cos(\beta_1 x) - \cosh(\beta_1 x))], \quad (9)$$

where C_1 represents a first modal shape amplitude, β_1 represents the constant of the 1st natural frequency defined as $\beta_1 = 1.875104/l$, l represents a beam length, and α_1 is defined as:

$$\alpha_1 = \frac{\sin \beta_1 l + \sinh \beta_1 l}{\cos \beta_1 l + \cosh \beta_1 l}. \quad (10)$$

Assuming the Euler–Bernoulli theory, the relationship between the bending moment and the curvature can be expressed as follows [71]:

$$M = E I \frac{d^2 W}{dx^2}, \quad (11)$$

where E is the elastic modulus, I is the area moment of inertia and M is the bending moment. The stress distribution over the cross-sectional area of a beam is given by the flexure formula [71]:

$$\sigma = \frac{M z}{I}, \quad (12)$$

where z represents the distance from the neutral axis.

Combining the above equations, the maximum stress distribution along the beam length in the first mode shape of the cantilever beam is obtained. Fig. 15 shows the normalized stress as a function of the relative beam length in the first mode shape.

Appendix C. Heating and cooling rates

Fig. 16 shows the heating rates and Fig. 17 shows the cooling rates for all tested materials.

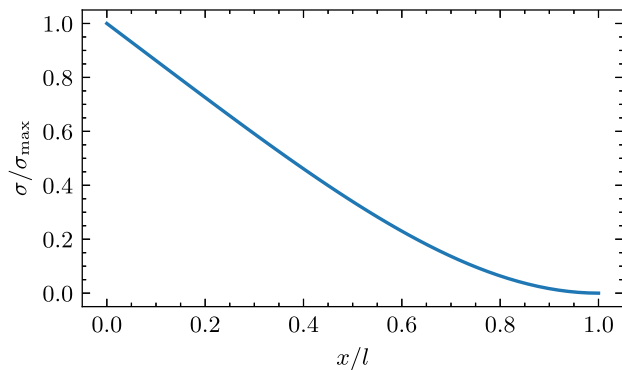
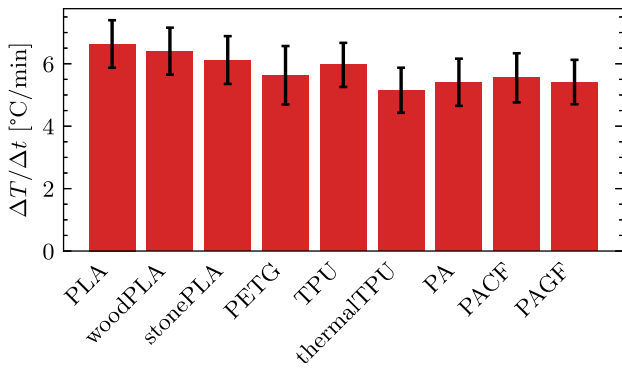
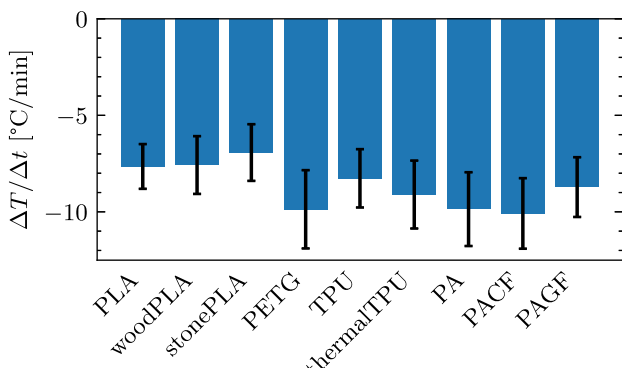
Appendix D. Range of natural frequencies for the calculation of the elastic modulus

Table 5 specifies the range of the measured first natural frequencies used for the calculation of the elastic modulus. Min f_1 was reached at the highest temperature during the experiment, and max f_1 at room temperature (lowest temperature).

Table 5

Range of measured first natural frequencies used to calculate elastic moduli.

Material	Beam length					
	40 mm		28 mm		20 mm	
	min f_1 [Hz]	max f_1 [Hz]	min f_1 [Hz]	max f_1 [Hz]	min f_1 [Hz]	max f_1 [Hz]
PLA	88.0	281.25	281.0	563.75	679.25	1027.25
woodPLA	88.0	218.75	89.5	433.75	252.5	807.0
stonePLA	88.5	349.5	88.0	675.75	109.25	1212.75
PETG	88.0	208.25	88.5	431.0	409.25	815.5
TPU	30.0	59.25	30.0	125.0	58.0	215.75
thermalTPU	30.0	79.75	30.0	154.75	67.75	282.0
PA	49.5	291.0	84.5	992.0	151.75	1331.0
PACF	88.0	481.75	90.25	787.0	279.25	1435.25
PAGF	88.0	289.25	136.25	575.5	340.75	1050.75

**Fig. 15.** Normalized stress vs. the relative length of a cantilever beam in the first mode shape.**Fig. 16.** Heating rates.**Fig. 17.** Cooling rates.

References

- [1] Z.X. Khoo, J.E.M. Teoh, Y. Liu, C.K. Chua, S. Yang, J. An, K.F. Leong, W.Y. Yeong, 3D printing of smart materials: A review on recent progresses in 4D printing, *Virtual Phys. Prototyp.* 10 (3) (2015) 103–122, <http://dx.doi.org/10.1080/17452759.2015.1097054>.
- [2] K.R. Ryan, M.P. Down, C.E. Banks, Future of additive manufacturing: Overview of 4D and 3D printed smart and advanced materials and their applications, *Chem. Eng. J.* 403 (2021) 126162, <http://dx.doi.org/10.1016/j.cej.2020.126162>.
- [3] Y. Ji, C. Luan, X. Yao, J. Fu, Y. He, Recent progress in 3D printing of smart structures: Classification, challenges, and trends, *Adv. Intell. Syst.* 3 (12) (2021) 2000271, <http://dx.doi.org/10.1002/aisy.202000271>.
- [4] T. Košir, J. Slavić, Single-process fused filament fabrication 3D-printed high-sensitivity dynamic piezoelectric sensor, *Addit. Manuf.* 49 (2022) 102482, <http://dx.doi.org/10.1016/j.addma.2021.102482>.
- [5] M. Arh, J. Slavić, Single-process 3D-printed triaxial accelerometer, *Adv. Mater. Technol.* 7 (7) (2022) 2101321, <http://dx.doi.org/10.1002/admt.202101321>.
- [6] T.B. Palmič, J. Slavić, Single-process 3D-printed stacked dielectric actuator, *Int. J. Mech. Sci.* 230 (2022) 107555, <http://dx.doi.org/10.1016/j.ijmecsci.2022.107555>.
- [7] P. Martins, D.M. Correia, V. Correia, S. Lanceros-Mendez, Polymer-based actuators: Back to the future, *Phys. Chem. Chem. Phys.* 22 (27) (2020) 15163–15182, <http://dx.doi.org/10.1039/DOPC02436H>.
- [8] T.B. Palmič, J. Slavić, Design principles for a single-process 3D-printed stacked dielectric actuators — Theory and experiment, *Int. J. Mech. Sci.* 246 (2023) 108128, <http://dx.doi.org/10.1016/j.ijmecsci.2023.108128>.
- [9] A. Zolfagharian, A.Z. Kouzani, S.Y. Khoo, A.A.A. Moghadam, I. Gibson, A. Kaynak, Evolution of 3D printed soft actuators, *Sensors Actuators A* 250 (2016) 258–272, <http://dx.doi.org/10.1016/j.sna.2016.09.028>.
- [10] K. Asaka, H. Okuzaki (Eds.), *Soft Actuators: Materials, Modeling, Applications, and Future Perspectives*, Springer Singapore, Singapore, 2019, <http://dx.doi.org/10.1007/978-981-13-6850-9>.
- [11] Y. Huang, J. Chen, M. Zhao, M. Feng, Electromechanical coupling characteristics of double-layer piezoelectric quasicrystal actuators, *Int. J. Mech. Sci.* 196 (2021) 106293, <http://dx.doi.org/10.1016/j.ijmecsci.2021.106293>.
- [12] X. Cao, S. Xuan, S. Sun, Z. Xu, J. Li, X. Gong, 3D printing magnetic actuators for biomimetic applications, *ACS Appl. Mater. Interfaces* 13 (25) (2021) 30127–30136, <http://dx.doi.org/10.1021/acsami.1c08252>.
- [13] C. Sano, M. Ataka, G. Hashiguchi, H. Toshiyoshi, An electret-augmented low-voltage MEMS electrostatic out-of-plane actuator for acoustic transducer applications, *Micromachines* 11 (3) (2020) 267, <http://dx.doi.org/10.3390/mi11030267>.
- [14] A. Zolfagharian, M.A.P. Mahmud, S. Gharai, M. Bodaghi, A.Z. Kouzani, A. Kaynak, 3D/4D-printed bending-type soft pneumatic actuators: Fabrication, modelling, and control, *Virtual Phys. Prototyp.* 15 (4) (2020) 373–402, <http://dx.doi.org/10.1080/17452759.2020.1795209>.
- [15] T. Hanuhov, N. Cohen, Thermally induced deformations in multi-layered polymeric struts, *Int. J. Mech. Sci.* 215 (2022) 106959, <http://dx.doi.org/10.1016/j.ijmecsci.2021.106959>.
- [16] Y. Tian, Y.-T. Li, H. Tian, Y. Yang, T.-L. Ren, Recent progress of soft electrothermal actuators, *Soft Robot.* 8 (3) (2021) 241–250, <http://dx.doi.org/10.1089/soro.2019.0164>.
- [17] A. Lendlein, O.E.C. Gould, Reprogrammable recovery and actuation behaviour of shape-memory polymers, *Nat. Rev. Mater.* 4 (2) (2019) 116–133, <http://dx.doi.org/10.1038/s41578-018-0078-8>.
- [18] V. Bučinskas, J. Subačiūtė-Žemaitienė, A. Dzedzickis, I. Morkvėnaitė-Vilkončienė, Robotic micromanipulation: A) actuators and their application, *Robot. Syst., Appl.* 1 (1) (2021) 2–23, <http://dx.doi.org/10.21595/rsa.2021.22071>.
- [19] Potekhina, Wang, Review of electrothermal actuators and applications, *Actuators* 8 (4) (2019) 69, <http://dx.doi.org/10.3390/act8040069>.
- [20] A. Zolfagharian, M. Lakhi, S. Ranjbar, Y. Tadesse, M. Bodaghi, 3D printing non-assembly compliant joints for soft robotics, *Results Eng.* 15 (2022) 100558, <http://dx.doi.org/10.1016/j.rineng.2022.100558>.

- [21] Y. Cao, J. Dong, High-performance low-voltage soft electrothermal actuator with directly printed micro-heater, *Sensors Actuators A* 297 (2019) 111546, <http://dx.doi.org/10.1016/j.sna.2019.111546>.
- [22] Y. Liu, S. Shang, S. Mo, P. Wang, B. Yin, J. Wei, Soft actuators built from cellulose paper: A review on actuation, material, fabrication, and applications, *J. Sci.: Adv. Mater. Devices* 6 (3) (2021) 321–337, <http://dx.doi.org/10.1016/j.jamd.2021.06.004>.
- [23] Y.-C. Sun, B.D. Leaker, J.E. Lee, R. Nam, H.E. Naguib, Shape programming of polymeric based electrothermal actuator (ETA) via artificially induced stress relaxation, *Sci. Rep.* 9 (1) (2019) 11445, <http://dx.doi.org/10.1038/s41598-019-47949-0>.
- [24] G. Tibi, E. Sachyani Kenneth, M. Layani, S. Magdassi, A. Degani, Three-layered design of electrothermal actuators for minimal voltage operation, *Soft Robot.* 7 (5) (2020) 649–662, <http://dx.doi.org/10.1089/soro.2018.0160>.
- [25] M.A. Aouraghe, Z. Mengjie, Y. Qiu, X. Fujun, Low-voltage activating, fast responding electro-thermal actuator based on carbon nanotube film/PDMS composites, *Adv. Fiber Mater.* 3 (1) (2021) 38–46, <http://dx.doi.org/10.1007/s42765-020-00060-w>.
- [26] S. Shin, H. So, Time-dependent motion of 3D-printed soft thermal actuators for switch application in electric circuits, *Addit. Manuf.* 39 (2021) 101893, <http://dx.doi.org/10.1016/j.addma.2021.101893>.
- [27] W.-H. Chu, M. Mehregany, R.L. Mullen, Analysis of tip deflection and force of a bimetallic cantilever microactuator, *J. Micromech. Microeng.* 3 (1) (1993) 4–7, <http://dx.doi.org/10.1088/0960-1317/3/1/002>.
- [28] Y. Li, Y. Chen, T. Ren, Y. Hu, Passive and active particle damping in soft robotic actuators, in: 2018 IEEE Int. Conf. Robot. Autom. ICRA, IEEE, Brisbane, QLD, Australia, 2018, pp. 1547–1552, <http://dx.doi.org/10.1109/ICRA.2018.8462895>.
- [29] J. Zhang, T. Wang, J. Wang, B. Li, J. Hong, J.X.J. Zhang, M.Y. Wang, Dynamic modeling and simulation of inchworm movement towards bio-inspired soft robot design, *Bioinspir. Biomim.* 14 (6) (2019) 066012, <http://dx.doi.org/10.1088/1748-3190/ab3e1f>.
- [30] D. Popescu, A. Zapciu, C. Amza, F. Baciu, R. Marinescu, FDM process parameters influence over the mechanical properties of polymer specimens: A review, *Polym. Test.* 69 (2018) 157–166, <http://dx.doi.org/10.1016/j.polymertesting.2018.05.020>.
- [31] D. Fico, D. Rizzo, R. Casciaro, C. Esposito Corcione, A review of polymer-based materials for fused filament fabrication (FFF): Focus on sustainability and recycled materials, *Polymers* 14 (3) (2022) 465, <http://dx.doi.org/10.3390/polym14030465>.
- [32] M. Ahmadifar, K. Benfriha, M. Shirinbayan, A. Tcharkhtchi, Additive manufacturing of polymer-based composites using fused filament fabrication (FFF): A review, *Appl. Compos. Mater.* 28 (5) (2021) 1335–1380, <http://dx.doi.org/10.1007/s10443-021-09933-8>.
- [33] M.Z. Khan, S.K. Srivastava, M. Gupta, A State-of-the-Art review on particulate wood polymer composites: Processing, properties and applications, *Polym. Test.* 89 (2020) 106721, <http://dx.doi.org/10.1016/j.polymertesting.2020.106721>.
- [34] Y. Yan, Y. Jiang, E.L.L. Ng, Y. Zhang, C. Owh, F. Wang, Q. Song, T. Feng, B. Zhang, P. Li, X.J. Loh, S.Y. Chan, B.Q.Y. Chan, Progress and opportunities in additive manufacturing of electrically conductive polymer composites, *Mater. Today Adv.* 17 (2023) 100333, <http://dx.doi.org/10.1016/j.mtadv.2022.100333>.
- [35] Á. Díaz-García, J.Y. Law, M. Felix, A. Guerrero, V. Franco, Functional, thermal and rheological properties of polymer-based magnetic composite filaments for additive manufacturing, *Mater. Des.* 219 (2022) 110806, <http://dx.doi.org/10.1016/j.mtades.2022.110806>.
- [36] I.M. Alarifi, PETG/Carbon fiber composites with different structures produced by 3D printing, *Polym. Test.* 120 (2023) 107949, <http://dx.doi.org/10.1016/j.polymertesting.2023.107949>.
- [37] G. Sodeifian, S. Ghaseminejad, A.A. Yousefi, Preparation of polypropylene/short glass fiber composite as fused deposition modeling (FDM) filament, *Results Phys.* 12 (2019) 205–222, <http://dx.doi.org/10.1016/j.rinp.2018.11.065>.
- [38] N. van de Werken, H. Tekinalp, P. Khanbolouki, S. Ozcan, A. Williams, M. Tehrani, Additively manufactured carbon fiber-reinforced composites: State of the art and perspective, *Addit. Manuf.* 31 (2020) 100962, <http://dx.doi.org/10.1016/j.addma.2019.100962>.
- [39] S. Kumar, M. Ramesh, M. Doddamani, S.M. Rangappa, S. Siengchin, Mechanical characterization of 3D printed MWCNTs/HDPE nanocomposites, *Polym. Test.* 114 (2022) 107703, <http://dx.doi.org/10.1016/j.polymertesting.2022.107703>.
- [40] M. Arif, H. Alhashmi, K. Varadarajan, J.H. Koo, A. Hart, S. Kumar, Multifunctional performance of carbon nanotubes and graphene nanoplatelets reinforced PEEK composites enabled via FFF additive manufacturing, *Composites B* 184 (2020) 107625, <http://dx.doi.org/10.1016/j.compositesb.2019.107625>.
- [41] Y. Zhao, Y. Chen, Y. Zhou, Novel mechanical models of tensile strength and elastic property of FDM AM PLA materials: Experimental and theoretical analyses, *Mater. Des.* 181 (2019) 108089, <http://dx.doi.org/10.1016/j.mtades.2019.108089>.
- [42] T. Yao, J. Ye, Z. Deng, K. Zhang, Y. Ma, H. Ouyang, Tensile failure strength and separation angle of FDM 3D printing PLA material: Experimental and theoretical analyses, *Composites B* 188 (2020) 107894, <http://dx.doi.org/10.1016/j.compositesb.2020.107894>.
- [43] Z. Liu, Q. Lei, S. Xing, Mechanical characteristics of wood, ceramic, metal and carbon fiber-based PLA composites fabricated by FDM, *J. Mater. Res. Technol.* 8 (5) (2019) 3741–3751, <http://dx.doi.org/10.1016/j.jmrt.2019.06.034>.
- [44] L. Pejkowski, J. Seyda, K. Nowicki, D. Mrozik, Mechanical performance of non-reinforced, carbon fiber reinforced and glass bubbles reinforced 3D printed PA12 polyamide, *Polym. Test.* 118 (2023) 107891, <http://dx.doi.org/10.1016/j.polymertesting.2022.107891>.
- [45] A. Sola, W.J. Chong, D. Pejak Simunec, Y. Li, A. Trinch, I.L. Kyratzi, C. Wen, Open challenges in tensile testing of additively manufactured polymers: A literature survey and a case study in fused filament fabrication, *Polym. Test.* 117 (2023) 107859, <http://dx.doi.org/10.1016/j.polymertesting.2022.107859>.
- [46] F. Medel, V. Esteban, J. Abad, On the use of laser-scanning vibrometry for mechanical performance evaluation of 3D printed specimens, *Mater. Des.* 205 (2021) 109719, <http://dx.doi.org/10.1016/j.mtades.2021.109719>.
- [47] B. Pszczółkowski, K.W. Nowak, W. Rejmer, M. Bramowicz, Ł. Dzadz, R. Gałecki, A comparative analysis of selected methods for determining Young's Modulus in polylactic acid samples manufactured with the FDM method, *Materials* 15 (1) (2021) 149, <http://dx.doi.org/10.3390/ma15010149>.
- [48] F. He, H. Ning, M. Khan, Effect of 3D printing process parameters on damping characteristic of cantilever beams fabricated using material extrusion, *Polymers* 15 (2) (2023) 257, <http://dx.doi.org/10.3390/polym15020257>.
- [49] M.Ö. Öteyaka, F.H. Çakir, M.A. Sofuoğlu, Effect of infill pattern and ratio on the flexural and vibration damping characteristics of FDM printed PLA specimens, *Mater. Today Commun.* 33 (2022) 104912, <http://dx.doi.org/10.1016/j.mtcomm.2022.104912>.
- [50] F. Medel, J. Abad, V. Esteban, Stiffness and damping behavior of 3D printed specimens, *Polym. Test.* 109 (2022) 107529, <http://dx.doi.org/10.1016/j.polymertesting.2022.107529>.
- [51] G. Morettini, M. Palmieri, L. Capponi, L. Landi, Comprehensive characterization of mechanical and physical properties of PLA structures printed by FFF-3D-printing process in different directions, *Prog. Addit. Manuf.* 7 (5) (2022) 1111–1122, <http://dx.doi.org/10.1007/s40964-022-00285-8>.
- [52] S. Wang, Y. Ma, Z. Deng, S. Zhang, J. Cai, Effects of fused deposition modeling process parameters on tensile, dynamic mechanical properties of 3D printed polylactic acid materials, *Polym. Test.* 86 (2020) 106483, <http://dx.doi.org/10.1016/j.polymertesting.2020.106483>.
- [53] I. Bute, S. Tarasovs, S. Vidinjevs, L. Vevere, J. Sevcenko, A. Aniskevich, Thermal properties of 3D printed products from the most common polymers, *Int. J. Adv. Manuf. Technol.* 124 (7–8) (2023) 2739–2753, <http://dx.doi.org/10.1007/s00170-022-10657-7>.
- [54] M. Qahtani, F. Wu, M. Misra, S. Gregori, D.F. Mielewski, A.K. Mohanty, Experimental design of sustainable 3D-printed poly(lactic acid)/biobased poly(butylene succinate) blends via fused deposition modeling, *ACS Sustain. Chem. Eng.* 7 (17) (2019) 14460–14470, <http://dx.doi.org/10.1021/acssuschemeng.9b01830>.
- [55] J.L. Faust, P.G. Kelly, B.D. Jones, J.D. Roy-Mayhew, Effects of coefficient of thermal expansion and moisture absorption on the dimensional accuracy of carbon-reinforced 3D printed parts, *Polymers* 13 (21) (2021) 3637, <http://dx.doi.org/10.3390/polym13213637>.
- [56] Y. Chen, L. Ye, A.J. Kinloch, Y. Zhang, 3D printed carbon-fibre reinforced composite lattice structures with good thermal-dimensional stability, *Compos. Sci. Technol.* 227 (2022) 109599, <http://dx.doi.org/10.1016/j.compscitech.2022.109599>.
- [57] N. Momenzadeh, C.M. Stewart, T. Berfield, Mechanical and thermal characterization of fused filament fabrication polyvinylidene fluoride (PVDF) printed composites, in: S. Kramer, J.L. Jordan, H. Jin, J. Carroll, A.M. Beese (Eds.), *Mechanics of Additive and Advanced Manufacturing*, Volume 8, Springer International Publishing, Cham, 2019, pp. 59–65, http://dx.doi.org/10.1007/978-3-319-95083-9_11.
- [58] C. Kousiata, D. Tzetzis, D. Karalekas, In-situ characterization of 3D printed continuous fiber reinforced composites: A methodological study using fiber Bragg grating sensors, *Compos. Sci. Technol.* 174 (2019) 134–141, <http://dx.doi.org/10.1016/j.compscitech.2019.02.008>.
- [59] N. Vidakis, M. Petousis, E. Velidakis, N. Mountakis, P.E. Fischer-Griffiths, S.A. Grammatikos, L. Tzounis, Fused filament fabrication 3D printed polypropylene/ alumina nanocomposites: Effect of filler loading on the mechanical reinforcement, *Polym. Test.* 109 (2022) 107545, <http://dx.doi.org/10.1016/j.polymertesting.2022.107545>.
- [60] G. Chapman, A.K. Pal, M. Misra, A.K. Mohanty, Studies on 3D printability of novel impact modified nylon 6: Experimental Investigations and performance evaluation, *Macromol. Mater. Eng.* 306 (2) (2021) 2000548, <http://dx.doi.org/10.1002/mame.202000548>.
- [61] S. Dul, L. Fambri, A. Pegoretti, Fused deposition modelling with ABS–Graphene nanocomposites, *Composites A* 85 (2016) 181–191, <http://dx.doi.org/10.1016/j.compositesa.2016.03.013>.
- [62] D. Moreno-Sánchez, A. Sanz de León, D. Moreno Nieto, F.J. Delgado, S.I. Molina, Basalt fiber composites with reduced thermal expansion for additive manufacturing, *Polymers* 14 (15) (2022) 3216, <http://dx.doi.org/10.3390/polym14153216>.

- [63] D. Fros, P. Vesely, Thermomechanical assessment of novel composites intended for fused deposition modeling, in: 2022 45th Int. Spring Semin. Electron. Technol. ISSE, IEEE, Vienna, Austria, 2022, pp. 1–8, <http://dx.doi.org/10.1109/ISSE54558.2022.9812709>.
- [64] N. Shahrubudin, T. Lee, R. Ramlan, An overview on 3D printing technology: Technological, materials, and applications, Procedia Manuf. 35 (2019) 1286–1296, <http://dx.doi.org/10.1016/j.promfg.2019.06.089>.
- [65] E. Cuan-Urquiza, E. Barocio, V. Tejada-Ortigoza, R. Pipes, C. Rodriguez, A. Roman-Flores, Characterization of the mechanical properties of FFF structures and materials: A review on the experimental, computational and theoretical approaches, Materials 12 (6) (2019) 895, <http://dx.doi.org/10.3390/ma12060895>.
- [66] R. Torre, S. Brischetto, Experimental characterization and finite element validation of orthotropic 3D-printed polymeric parts, Int. J. Mech. Sci. 219 (2022) 107095, <http://dx.doi.org/10.1016/j.ijmecsci.2022.107095>.
- [67] M.F. Ashby, D.R. Jones, The elastic moduli, in: Engineering Materials, Vol. 1, Elsevier, 2012, pp. 29–53, <http://dx.doi.org/10.1016/B978-0-08-096665-6.00003-9>.
- [68] S.S. Rao, Mechanical Vibrations, sixth ed., Pearson, Hoboken, 2017.
- [69] J. He, Z.-F. Fu, Modal Analysis, Butterworth-Heinemann, Oxford ; Boston, 2001.
- [70] C.Y. Ho, R.E. Taylor, Thermal Expansion of Solids, ASM International, Materials Park, Ohio, 1998.
- [71] R.C. Hibbeler, Mechanics of Materials, tenth edition in SI units, global ed., Pearson, Harlow, 2018.
- [72] N. McCormick, J. Lord, Digital image correlation, Mater. Today 13 (12) (2010) 52–54, [http://dx.doi.org/10.1016/S1369-7021\(10\)70235-2](http://dx.doi.org/10.1016/S1369-7021(10)70235-2).
- [73] H. Schreier, J.-J. Orteu, M.A. Sutton, Image Correlation for Shape, Motion and Deformation Measurements, Springer US, Boston, MA, 2009, <http://dx.doi.org/10.1007/978-0-387-78747-3>.
- [74] B. Pan, Recent progress in digital image correlation, Exp. Mech. 51 (7) (2011) 1223–1235, <http://dx.doi.org/10.1007/s11340-010-9418-3>.
- [75] B. Pan, K. Qian, H. Xie, A. Asundi, Two-dimensional digital image correlation for in-plane displacement and strain measurement: A review, Meas. Sci. Technol. 20 (6) (2009) 062001, <http://dx.doi.org/10.1088/0957-0233/20/6/062001>.
- [76] A. Shrivastava, Introduction to Plastics Engineering, Elsevier, 2018, pp. 1–16, <http://dx.doi.org/10.1016/B978-0-323-39500-7.00001-0>.
- [77] K.P. Menard, N.R. Menard, Dynamics Mechanical Analysis, third ed., CRC Press, 2020, <http://dx.doi.org/10.1201/9780429190308>.
- [78] A. Labuschagne, N. van Rensburg, A. van der Merwe, Comparison of linear beam theories, Math. Comput. Modelling 49 (1–2) (2009) 20–30, <http://dx.doi.org/10.1016/j.mcm.2008.06.006>.
- [79] C. Truong, L. Oudre, N. Vayatis, Selective review of offline change point detection methods, Signal Process. 167 (2020) 107299, <http://dx.doi.org/10.1016/j.sigpro.2019.107299>.